Aalborg Universitet

AALBORG UNIVERSITY

Analysis and design of grid-current-feedback active damping for LCL resonance in grid-connected voltage source converters

Wang, Xiongfei; Blaabjerg, Frede; Loh, Poh Chiang

Analysis and Design of Grid-Current-Feedback Active Damping for *LCL* Resonance in Grid-Connected Voltage Source Converters

Xiongfei Wang, Frede Blaabjerg, Poh Chiang Loh
Department of Energy Technology, Aalborg University, Aalborg, Denmark
xwa@et.aau.dk, fbl@et.aau.dk, pcl@et.aau.dk

Abstract—**This paper investigates the active damping of *LCL*-filter resonance within single-loop grid current control of grid-connected voltage source converters. First, the basic analysis in the continuous *s*-domain reveals that the grid-current-feedback active damping forms a virtual impedance across the grid-side inductor, and the use of a high-pass filter with a negative sign shapes the virtual impedance by an *RL* damper paralleled by a negative inductance. It is further found that such a negative virtual inductance plays a critical role in mitigating the phase lag caused by the time delay in a digital control system. The instability induced by the negative virtual resistance, which is commonly experienced in the feedback-type active damping, can thus be avoided. A systematic design method of the high-pass filter is also proposed by the help of root locus analysis in the discrete *z*-domain. Lastly, experimental tests are presented to validate the theoretical analysis.**

I. INTRODUCTION

LCL resonance has always been an important concern for *LCL*-filtered voltage source converters [1]. A wide variety of resonance damping technologies have been reported, among which active damping control methods are usually preferred over passive dampers in order to avoid extra power losses [2]. Generally, the active damping can be attained either by introducing a digital filter in cascade with current controller [3], or based on the feedback of filter state variables [4]-[16].

Plugging-in digital filters provides a sensorless damping, but it is sensitive to parameter uncertainties [10]. Feedback-type active damping have therefore attracted more attentions with filter capacitor current or voltage feedback being well documented [4]-[9]. However, these schemes often require an additional sensor or observer-based control [6]. Moreover, the performance of the feedback-type active damping may be influenced by the transport delay in a digital control system, which may insert a negative virtual resistance. This will add open-loop Right-Half-Plane (RHP) poles in the control loop, resulting in a non-minimum phase behavior in the closed-

loop response [7]. In [8], a High-Pass Filter (HPF) instead of a proportional gain is introduced within the capacitor current feedback, in order to avoid the non-minimum phase system resulting from the synthesis of negative virtual resistance.

To obtain a robust damping with a minimum number of sensors, the single-loop current control has increasingly been studied [9]-[16]. It is shown in [11] that a stable grid current control can be achieved without damping. This is due to the inherent damping effect of transport delay when grid current is controlled, which however requires that the *LCL* resonance frequency is above the one-sixth of the system sampling frequency [9], [12]. In weak power grids, the *LCL* resonance frequency may shift in a wide range with the variation of grid impedance, thus external damping is still needed for robust current control. This issue may be more challenging in the emerging power-electronics-based power systems, where the interactions of multiple converters may lead to harmonic instability [13].

It is therefore of interest to develop active damping with grid current feedback control [14]-[16]. Unlike the capacitor current feedback through a proportional gain, the s^2 term is needed for the virtual resistive damping, which is difficult to implement in digital or analog controllers. Hence, a second-order Infinite Impulse Response (IIR) filter [14] or a first-order HPF with a negative sign [15], [16] has been reported to replace the s^2 term. Since the HPF is easier to implement than the IIR filter, it is becoming more attractive. Parameter design of the HPF has been discussed in [15], [16], but how the HPF is influenced by the transport delay is not identified. Moreover, due to the lack of physical meaning of the HPF, the non-minimum phase characteristic of the control system caused by the negative virtual resistance is overlooked.

This paper proposes first an impedance-based analysis in the continuous *s*-domain to generalize the physical property of the grid current feedback active damping. It reveals that the grid current feedback basically forms a virtual impedance in parallel with the grid-side inductor, and the use of HPF with a negative sign furnishes a virtual *RL* damper in parallel

with a negative inductance. Then, taking the transport delay into account, the resistance of the *RL* damper may turn into negative, which will lead to a non-minimum phase behavior in the control loop, impairing the system stability robustness. On the other hand, it is also found that the negative virtual inductance helps to mitigate the negative resistance with a proper design of the HPF. Consequently, the frequency region for the negative virtual resistance is identified, which is dependent on the ratio of the HPF cutoff frequency to the sampling frequency. Hence, to obtain a robust damping, a systematic design of the HPF is developed by means of root locus analysis in the discrete *z*-domain. Experimental results are presented to validate the theoretical analyses.

II. IMPEDANCE-BASED ANALYSIS

A. System Description

Fig. 1 shows a three-phase grid-connected voltage source converter with an *LCL* filter. The DC-link voltage V_{dc} of the converter can be treated as constant for simplicity. Parasitic resistances in the circuit are neglected for the worst case of stability. The Synchronous Reference Frame-Phase-Locked Loop (SRF-PLL) is used to synchronize the converter with the Point of Common Coupling (PCC) voltage [17], whose bandwidth is designed as smaller than the grid fundamental frequency to avoid the undesired low-frequency instability [18]. The grid voltage V_g is assumed as three-phase balanced, which allows using the per-phase diagram for analysis.

Fig. 2 depicts the per-phase block diagram of grid current control loop, where the grid current i_2 is controlled for both power flow regulation and active damping of *LCL* resonance. $G_c(s)$ is the current controller, which is implemented with a Proportional Resonant (PR) controller in the stationary $\alpha\beta$-frame [9]. $G_{ad}(s)$ is the active damping controller.

$$G_c(s) = k_p + \frac{k_i s}{s^2 + \omega_1^2} \qquad (1)$$

where ω_1 is the grid fundamental frequency. Both of them are influenced by the time delay in a digital control system $G_d(s)$, which can simply be approximated as follow [19]:

$$G_d(s) = e^{-1.5 T_s s} \qquad (2)$$

where T_s is the system sampling period.

B. Impedance-Based Equivalent Circuits

To illustrate the general physical property of grid current feedback active damping, an equivalent block diagram of the grid current control is derived in Fig. 3 (a). This is obtained by replacing grid current with the grid-side inductor voltage, and moving the summing point at the output of PR controller to the output of the transfer function of the converter-side inductor L_1. Thus, it is shown that the grid current feedback damping basically forms a virtual impedance $Z_v(s)$ in parallel with the grid-side inductor L_2. This notation is drawn in Fig. 3 (b) and is expressed in (3).
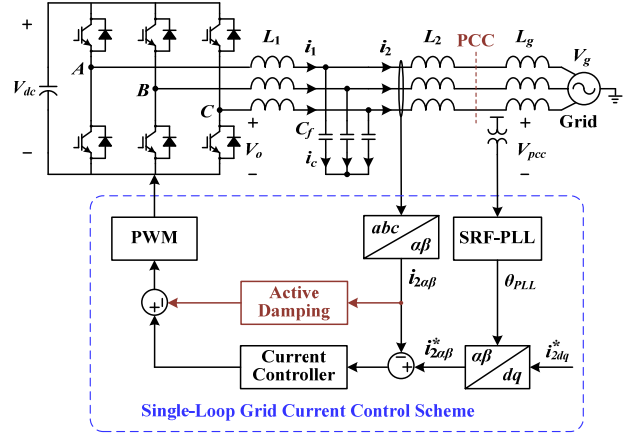
Consequently, the required controllers for different forms

Fig. 1. Three-phase grid-connected, *LCL*-filtered voltage source converter with the single-loop grid current control scheme.
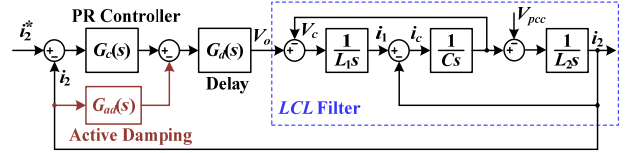

Fig. 2. Per-phase block diagram of the grid current control loop.

(a)

(b)
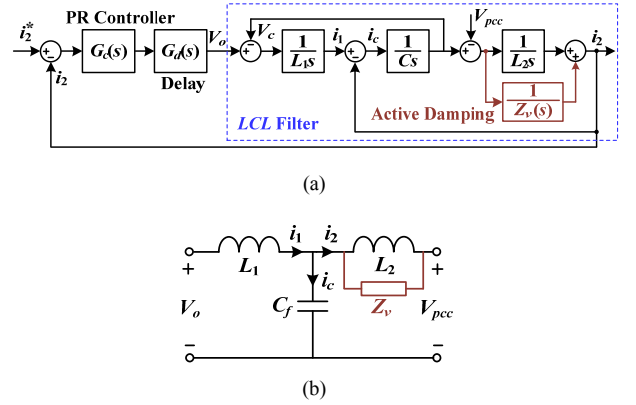
Fig. 3. Equivalent control diagram and the generalized equivalent circuit of *LCL* filter. (a) Control diagram. (b) *LCL* filter circuit.

$$Z_v(s) = \frac{L_1 L_2 s^2}{G_{ad}(s) G_d(s)} \qquad (3)$$

of virtual impedance $Z_v(s)$ can be derived based on (3), and the impact of the transport delay $G_d(s)$ can be identified.

First, the influence of the system delay $G_d(s)$ is nullified to generalize the virtual impedances formed by the different $G_{ad}(s)$, which are collectively shown in Fig. 4. The s^2 term is needed in $G_{ad}(s)$ to shape $Z_v(s)$ as the resistance shown in Fig. 4 (a), which complicates the controller design. Hence, it is of interest to form a first-order *RL* damper as shown in Fig. 4 (b) in order to avoid the use of s^2 term in $G_{ad}(s)$. As

Fig. 4. Virtual impedance-based equivalent circuits of grid current active damping loop with different controllers $G_{ad}(s)$. (a) Single resistance. (b) Series *RL* damper. (c) Series *RL* damper in parallel with –*L*.
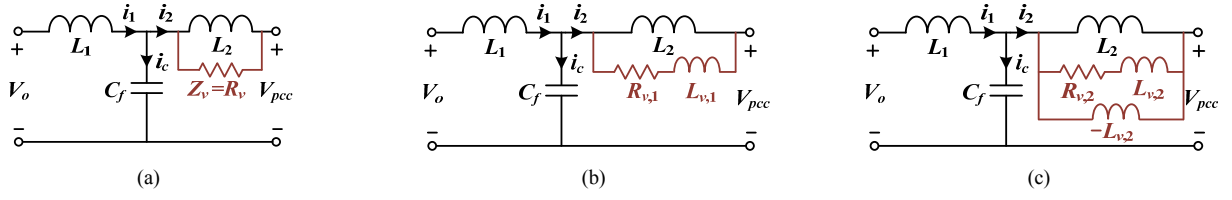
derived in (4) and (5), $G_{ad}(s)$ is then composed by a first-order derivative term and a HPF with the negative sign.

$$Z_{v,1}(s) = L_{v,1}s + R_{v,1} \tag{4}$$

$$G_{ad,1}(s) = \frac{L_1 L_2 s^2}{L_{v,1}s + R_{v,1}} = \frac{L_1 L_2 s}{L_{v,1}} - \frac{L_1 L_2 R_{v,1}s}{L_{v,1}(L_{v,1}s + R_{v,1})} \tag{5}$$

where $L_{v,1}$ and $R_{v,1}$ are the virtual inductance and resistance of the virtual *RL* damper.

In contrast, using the HPF with the negative sign only, which has earlier been used in [15], [16], will add a negative virtual inductance (–*L*) in parallel with the *RL* damper, as shown in Fig. 4 (c). Consequently, $G_{ad}(s)$ can be given by

$$Z_{v,2}(s) = \frac{-L_{v,2}s(L_{v,2}s + R_{v,2})}{R_{v,2}} \Rightarrow G_{ad,2}(s) = \frac{-L_1 L_2 R_{v,2}s}{L_{v,2}(L_{v,2}s + R_{v,2})} \tag{6}$$

$$G_{ad,2}(s) = \frac{-k_{ad}s}{s + \omega_{ad}} \Rightarrow k_{ad} = \frac{L_1 L_2 R_{v,2}}{L_{v,2}^2}, \quad \omega_{ad} = \frac{R_{v,2}}{L_{v,2}} \tag{7}$$

where ω_{ad} and k_{ad} are the cutoff frequency and gain of the HPF, respectively. $L_{v,2}$ and $R_{v,2}$ are the virtual inductance and resistance furnished by the HPF. It is interesting to note that if the virtual inductance is chosen as the grid-side inductor L_2, the equivalent circuit in Fig. 4 (c) will be simplified as a $R_{v,2}$ in series with L_2, and k_{ad} will be equal to $\omega_{ad}L_1$.

Then, with the delay included, the virtual impedance in (4) and (6) are changed as follows

$$Z_{v,1d} = (R_{v,1} + j\omega L_{v,1})\left[\cos(1.5T_s\omega) + j\sin(1.5T_s\omega)\right] \tag{8}$$

$$\mathrm{Re}\{Z_{v,1d}\} = R_{v,1}\cos(1.5T_s\omega) - \omega L_{v,1}\sin(1.5T_s\omega)$$
$$\mathrm{Im}\{Z_{v,1d}\} = R_{v,1}\sin(1.5T_s\omega) + \omega L_{v,1}\cos(1.5T_s\omega) \tag{9}$$

$$Z_{v,2d} = \left(\frac{L_{v,2}^2\omega^2}{R_{v,2}} - j\omega L_{v,2}\right)\left[\cos(1.5T_s\omega) + j\sin(1.5T_s\omega)\right] \tag{10}$$

$$\mathrm{Re}\{Z_{v,2d}\} = \frac{L_{v,2}^2\omega^2}{R_{v,2}}\cos(1.5T_s\omega) + \omega L_{v,2}\sin(1.5T_s\omega)$$
$$\mathrm{Im}\{Z_{v,2d}\} = \frac{L_{v,2}^2\omega^2}{R_{v,2}}\sin(1.5T_s\omega) - \omega L_{v,2}\cos(1.5T_s\omega) \tag{11}$$

From (9) and (11), it is seen that both the imaginary and real terms of the virtual impedance can become negative due to the effect of transport delay. The negative imaginary term reduces the actual *LCL* resonance frequency ω_{res}, while the negative real term adds open-loop RHP poles to the current control loop and results in a non-minimum phase response. Moreover, comparing the real terms in (10) and (12), it can be found that the negative virtual inductance (–$L_{v,2}$) in Fig. 4 (c) lessens the likelihood of $\mathrm{Re}\{Z_{v,2}\}$ being negative than the *RL* damper given in Fig. 4 (b). This is a prominent feature of the negative virtual inductance furnished by the HPF, which is however overlooked in [15], [16].

It is therefore important to identify the critical frequency ω_v, above which $\mathrm{Re}\{Z_{v,2d}\}$ turns into negative. This can be derived by replacing the *RL* constants in (12) with the HPF parameters, which are given in the following

$$\mathrm{Re}\{Z_{v,2d}\} = \frac{L_1 L_2 \omega^2}{k_{ad}}\cos(1.5T_s\omega) + \frac{L_1 L_2 \omega_{ad}\omega}{k_{ad}}\sin(1.5T_s\omega) \tag{12}$$

$$\mathrm{Re}\{Z_{v,2d}\} = 0 \Rightarrow \frac{\omega_v}{\omega_s}\cos\left(\frac{3\pi\omega_v}{\omega_s}\right) + \frac{\omega_{ad}}{\omega_s}\sin\left(\frac{3\pi\omega_v}{\omega_s}\right) = 0 \tag{13}$$

where $\omega_s = 2\pi f_s$, f_s is the sampling frequency. Consequently, a relationship between the critical frequency ω_v and the HPF cutoff frequency ω_{ad} can be obtained.

Fig. 5 plots the critical frequency ω_v in terms of the HPF cutoff frequency ω_{ad}. At $\omega_{ad} = 0$, $G_{ad,2}(s)$ turns as a negative
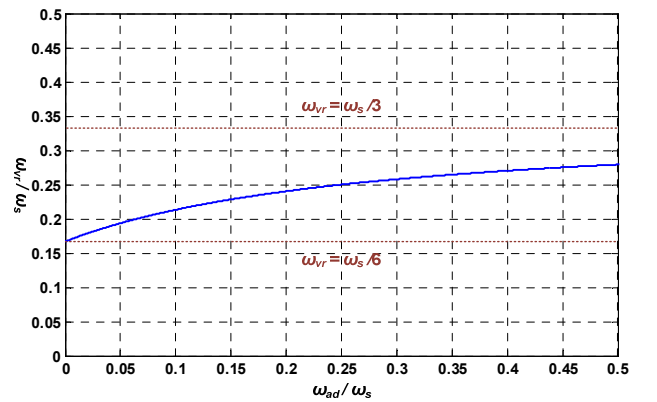

Fig. 5. Relationship between critical frequency ω_v and the cutoff frequency of the HPF ω_{ad}.

proportional gain, $\omega_v = \omega_s/6$, which implies that the positive proportional gain is needed for the *LCL* resonance frequency $\omega_{res} > \omega_s/6$. It agrees with the stability analysis of the grid current control [9], [12]. Above $\omega_{ad} = 0$, ω_v increases with ω_{ad}, and saturates at $\omega_s/3$, since the $\sin(3\pi\omega_v/\omega_s)$ term in (13) is equal to zero at $\omega_v = \omega_s/3$. Hence, for $\omega_s/6 < \omega_{res} < \omega_s/3$, the insertion of the negative virtual resistance can be avoided by selecting ω_{ad} that gives a good margin between ω_{res} and ω_v, whereas for $\omega_{res} > \omega_s/3$, the synthesis of the negative virtual resistance is inevitable. This is an inherent limit in this HPF-based active damping scheme. On the other hand, in order to avoid the noise amplification with the HPF or the digital sampling error, ω_{ad} is generally chosen as lower than the Nyquist frequency of the digital control system. Hence, the ω_v corresponding to $\omega_{ad} = 0.5\omega_s$ is normally the upper limit of ω_{res} in order to avoid the non-minimum phase dynamic.

III. DISCRETE *z*-DOMAIN ANALYSIS

To confirm the impedance-based analysis and to illustrate the design of controller parameters, the root locus analysis in the discrete *z*-domain is presented in the following. Table I lists the main circuit parameters adopted in this work, where three filter capacitor values corresponding to three different filter resonance frequencies are considered.

A. Discrete z-Domain Model

Fig. 6 illustrates the grid current control diagram in the discrete *z*-domain, where $L_t = L_2 + L_g$. The Zero-Order Hold (ZOH) is used to model the delay induced by the Digital Pulse Width Modulation (DPWM). The one sampling period of computation delay is included as z^{-1} [19]. Hence, the transfer function $Y_g(s)$ in (14), which relates the converter output voltage V_o to the grid current i_2, is discretized by the ZOH transformation in (15).

$$Y_g(s) = \frac{i_2}{V_o}\bigg|_{V_g=0} = \frac{1}{L_1 L_t C_f s\left(s^2 + \omega_{res}^2\right)}, \quad \omega_{res} = \sqrt{\frac{L_1 + L_t}{L_1 L_t C}} \quad (14)$$

$$Y_g(z) = \frac{T_s}{(L_1 + L_t)(z-1)} - \frac{(z-1)\sin(\omega_{res}T_s)}{\omega_{res}(L_1 + L_t)\left[z^2 - 2z\cos(\omega_{res}T_s) + 1\right]} \quad (15)$$

The PR controller is discretized by the Tustin transformation with the pre-warping at the grid fundamental frequency [20], and the HPF is discretized by the Tustin transformation only.

$$G_c(z) = k_p + k_i \frac{\sin(\omega_1 T_s)}{2\omega_1} \frac{z^2 - 1}{z^2 - 2z\cos(\omega_1 T_s) + 1} \quad (16)$$

$$G_{ad,2}(z) = \frac{2k_{ad}(1-z)}{(\omega_{ad}T_s + 2)z + \omega_{ad}T_s - 2} \quad (17)$$

Consequently, the open-loop gain of the grid current control loop, denoted as $T_{ol}(z)$, and the resulting closed-loop transfer function $T_{cl}(z)$ can be derived based on (15) to (17), which are given in (18) and (19).

TABLE I.   MAIN CIRCUIT PARAMETERS

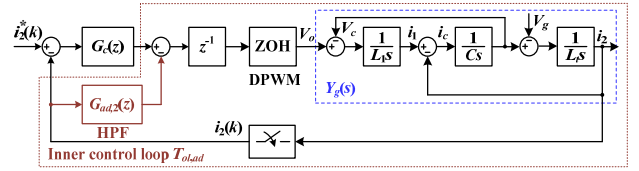| Symbol	Electrical Constant	Value
V_g	Grid voltage	400 V
f_1	Grid fundamental frequency	50 Hz
f_{sw}	Switching frequency	10 kHz
f_s	Sampling frequency	10 kHz
V_{dc}	DC-link voltage	750 V
L_1	Converter-side filter inductor	1.8 mH
L_2	Grid-side filter inductor	1 mH
C_f	Filter capacitor	4.7/9.4/13.5 μF
L_g	Grid inductance	0.8 mH

Fig. 6. Block diagram of grid current control loop in the discrete *z*-domain.

$$T_{ol}(z) = \frac{z^{-1}G_c(z)Y_g(z)}{1 + z^{-1}G_{ad,2}(z)Y_g(z)} \quad (18)$$

$$T_{cl}(z) = \frac{z^{-1}G_c(z)Y_g(z)}{1 + z^{-1}\left[G_c(z) + G_{ad,2}(z)\right]Y_g(z)} \quad (19)$$

B. Negative Virtual Resistance – Unstable Active Damping

From Fig. 6, it is seen that $G_{ad,2}(z)$ forms an inner active damping control loop to reshape the *LCL* filter, and the open-loop gain is given by

$$T_{ol,ad}(z) = z^{-1}G_{ad,2}(z)Y_g(z) \quad (20)$$

The insertion of the negative virtual resistance will result in an unstable active damping control loop. Hence, the presence of the negative virtual resistance can be identified by the root locus analysis of the inner control loop.

Fig. 7 shows the root loci of the inner control loop based on the open-loop gain given in (20). Notice that these root loci are also the open-loop poles trajectories of the outer grid current control loop. The unstable active damping indicates a non-minimum phase behavior of the current control loop. Two different *LCL* resonance frequencies are compared, which are corresponding to $C_f = 4.7$ μF, $\omega_{res} = 0.24\omega_s$ in Fig. 7 (a), and $C_f = 9.4$ μF, $\omega_{res} = 0.17\omega_s$ in Fig. 7 (b). The HPF cutoff frequency ω_{ad} is swept from 0 to $0.5\omega_s$ with a step of $0.05\omega_s$. It can be seen that the root loci initially track outside the unit circle, and are then forced to move inside the unit circle as the increase of the HPF cutoff frequency ω_{ad}.

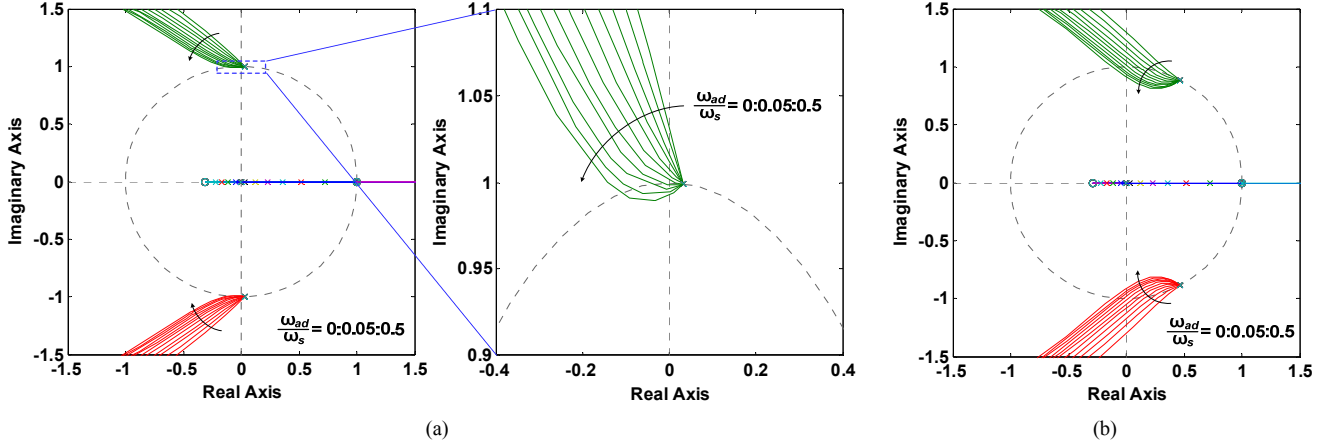Fig. 7 (a) shows that the root loci are kept outside the unit

Fig. 7. Root loci of the active damping control loop without the PR current controller. (a) $C_f = 4.7$ μF, $\omega_{res} = 0.24\omega_s$. (b) $C_f = 9.4$ μF, $\omega_{res} = 0.17\omega_s$.

circle before $\omega_{ad} > 0.3\omega_s$, while for the low ω_{res} case in Fig. 7 (b), the root loci move into the unit circle since $\omega_{ad} > 0.5\omega_s$. Such phenomena indicate that the ω_{res} needs to be below the critical frequency ω_v, which is determined by ω_{ad}, to avoid unstable active damping. Compared to the critical frequency identified by the impedance-based models in Fig. 5, a good match with the root loci analysis is obtained.

C. Co-Design of Active Damping and Current Controllers

Traditionally, the grid current controller is first designed based on the total inductance (L_1+L_t) and the desired phase margin θ_m, which are given as follows [21]

$$\omega_c = \frac{\pi - 2\theta_m}{3T_s}, \quad k_p = \omega_c(L_1 + L_t), \quad k_i = \frac{\omega_c}{10} \quad (21)$$

where ω_c is the crossover frequency of the current control loop. Then, the active damping controller is designed based on the system with the current controller by using either root locus analysis or analytical equations [8], [9], [15]. Such a design flow is easy to implement, but overlooks the effect of active damping controller on the filter shaping.

Figs. 8 to 10 show the closed-loop pole trajectory under the different *LCL* resonance frequencies, where three cutoff frequencies ($\omega_{ad} = 0.15\omega_s, 0.25\omega_s, 0.35\omega_s$) and four gains ($k_{ad} = 0, 5, 15, 35$) of the HPF are shown. Beginning with Fig. 8 for $C_f = 4.7$ μF, $\omega_{res} = 0.24\omega_s$, it is seen that the closed-loop poles track inside the unit circle for $k_{ad} = 0$, where no damping is added. This is due to the inherent damping effect of the transport delay for $\omega_{res} > \omega_s/6$. As for $k_{ad} \neq 0$, the root loci are moving inside the unit circle as the increase of ω_{ad}, which implies that the use of active damping can improve the transient performance of the control system, even if there is no need for resonance damping. However, the increase of k_{ad} forces a pair of open-loop poles to move even far from the unit circle, and pushes the root loci outwards the unit circle. As shown in Fig. 8 (a), the system becomes unstable for $k_{ad} = 35$, no matter how to design the current controller with this structure. The non-minimum phase characteristic will also bring in a lower stable limit for the proportional gain of the current controller k_p, which tends to make more impact when ω_{res} is above the critical frequency ω_v.

In contrast, Figs. 9 and 10 show the root loci for the cases of low *LCL* resonance frequencies, where the ω_{res} is close to
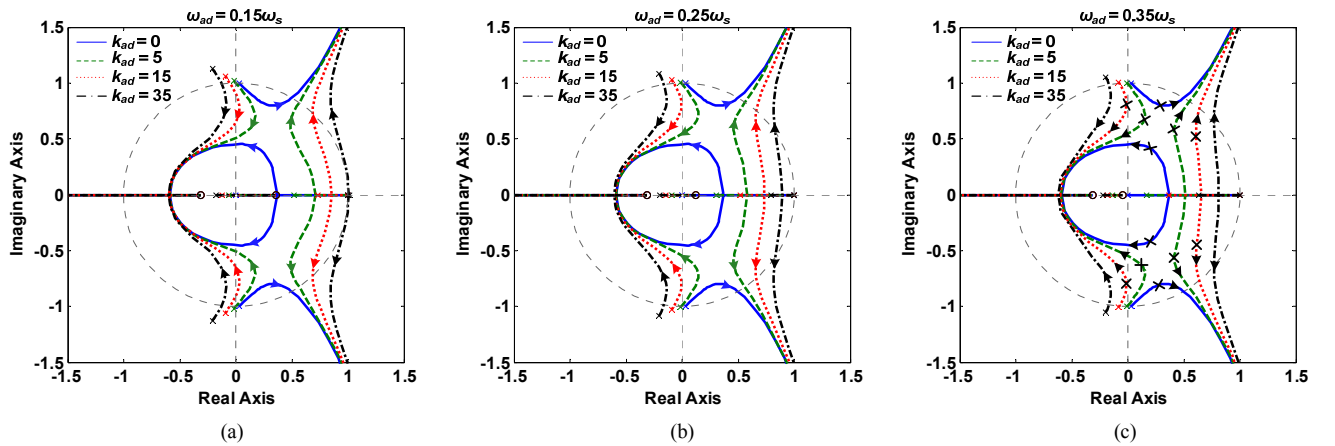

Fig. 8. Root loci of grid current control loop for $C_f = 4.7$ μF, $\omega_{res} = 0.24\omega_s$. (a) $\omega_{ad} = 0.15\omega_s$. (b) $\omega_{ad} = 0.25\omega_s$. (c) $\omega_{ad} = 0.35\omega_s$.

Fig. 9. Root loci of grid current control loop for $C_f = 9.4\ \mu F$, $\omega_{res} = 0.17\omega_s$. (a) $\omega_{ad} = 0.15\omega_s$. (b) $\omega_{ad} = 0.25\omega_s$. (c) $\omega_{ad} = 0.35\omega_s$.

Fig. 10. Root loci of grid current control loop for $C_f = 14.1\ \mu F$, $\omega_{res} = 0.14\omega_s$. (a) $\omega_{ad} = 0.15\omega_s$. (b) $\omega_{ad} = 0.25\omega_s$. (c) $\omega_{ad} = 0.35\omega_s$.
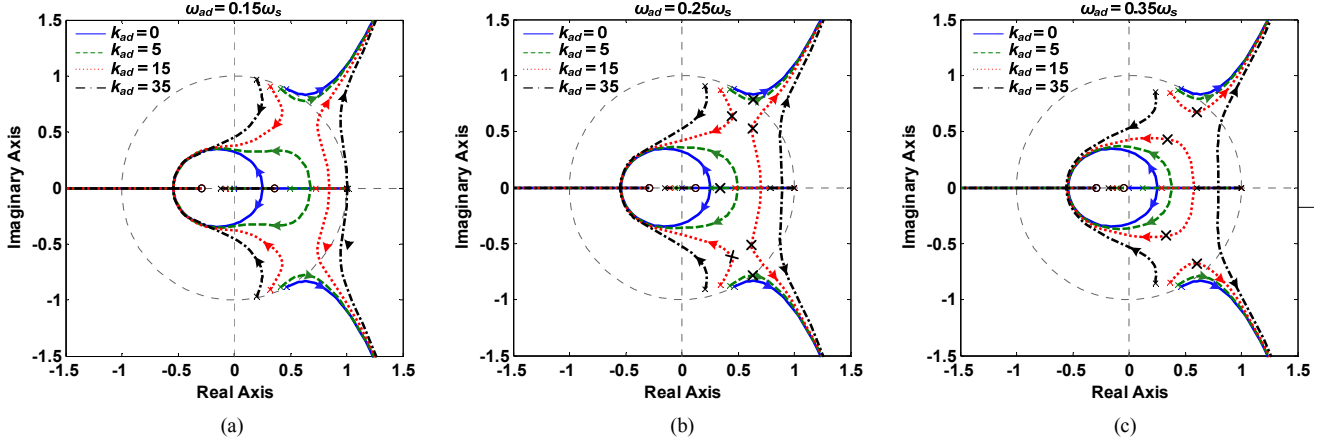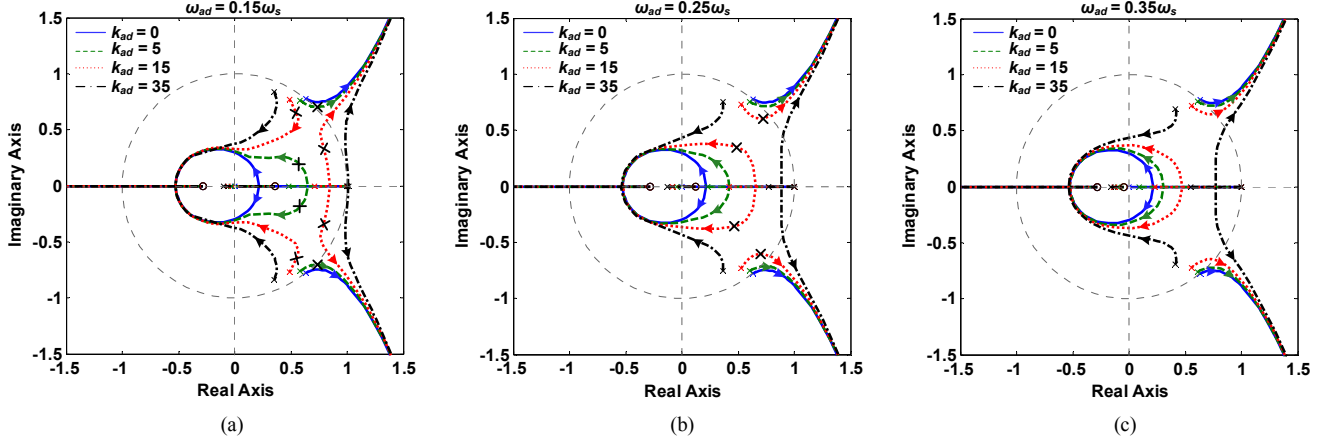
$\omega_s/6$ in Fig. 9, and $\omega_{res} < \omega_s/6$ in Fig. 10. In both cases, the closed-loop poles track outside the unit circle for $k_{ad} = 0$. It is therefore needed to adopt the active damping to stabilize the control system. Unlike Fig. 8, there are no open-loop poles outside the unit circle in Figs. 9 and 10. Only for $\omega_{ad} = 1.5\omega_s$ in Fig. 9(a) and Fig. 10(a), the open-loop poles are moving outwards the unit circle with the increase of k_{ad}, and the system turns unstable for $k_{ad} = 35$, no matter how to design the current controller with the given structure. Moreover, the increase of ω_{ad} does not always force the root loci to move inside the unit circle. As for $k_{ad} = 15$ shown in Fig. 9 (c), Figs. 10 (b) and (c), a higher ω_{ad} is moving the root locus outwards the unit circle, which leads to less damping. Hence, for the different filter capacitors, the parameters of the active damping controller for the optimal root locus are different. Consequently, the proportional gain of the current controller for the optimal damping poles will be different. Designing the current controller merely based on the total inductance may not yield optimal parameters.

A co-design of the HPF and the proportional gain of grid current controller k_p by the root locus analyses like in Figs. 8 to 10 is therefore needed. The design flow is summarized as follows:

1) The HPF cutoff frequency can be determined based on Fig. 5 to avoid introducing the non-minimum phase system.

2) Then, a set of HPF parameters like in Figs. 8 to 10 can be used to identify their influences on the root loci of the control system, and consequently select their parameters for the optimal root locus.

3) Lastly, the proportional gain of the current controller is determined for the optimal damping based on the locations of poles. Since the resonant integral gain of current controller only works at the grid fundamental frequency, it can still be designed by following the traditional method in (21).

IV. EXPERIMENTAL RESULTS

To confirm the theoretical analyses presented, the three-phase voltage source converter in Fig. 1 is implemented and connected to a *California Instruments* MX-series AC power supply for grid emulation. Circuit parameters listed in Table I are chosen for the converter. Table II gives the parameters designed for the controllers following the analyses in Figs. 8 to 10. The corresponding closed-loop poles are highlighted

Test Case	PR controller (k_p)	PR controller (k_i)	HPF (ω_{ad})	HPF (k_{ad})
Case I C_f = 4.7 μF, ω_{res} = 0.24ω_s	16	600	0.35ω_s	0/5/15
Case II C_f = 9.4 μF, ω_{res} = 0.17ω_s	12	600	0.25ω_s/0.35ω_s	5/15
Case III C_f = 14.1 μF, ω_{res} = 0.14ω_s	9	600	0.15ω_s/0.25ω_s	5/15

(a)   (b)   (c)

Fig. 11. Measured A-phase grid voltage and grid current for C_f = 4.7 μF, ω_{res} = 0.24ω_s. (a) k_{ad} = 0. (b) k_{ad} = 5, ω_{ad} = 0.35ω_s. (c) k_{ad} = 15, ω_{ad} = 0.35ω_s.

(a)   (b)   (c)
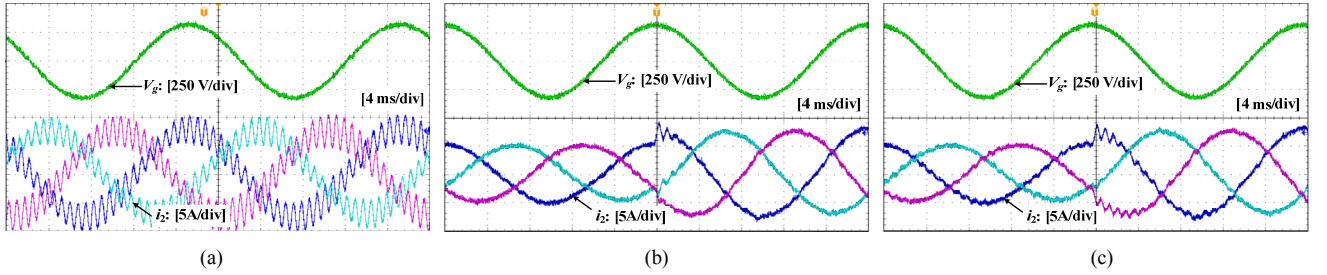
Fig. 12. Measured A-phase grid voltage and grid current for C_f = 9.4 μF, ω_{res} = 0.17ω_s. (a) k_{ad} = 5, ω_{ad} = 0.25ω_s. (b) k_{ad} = 15, ω_{ad} = 0.25ω_s. (c) k_{ad} = 15, ω_{ad} = 0.35ω_s.

(a)   (b)   (c)
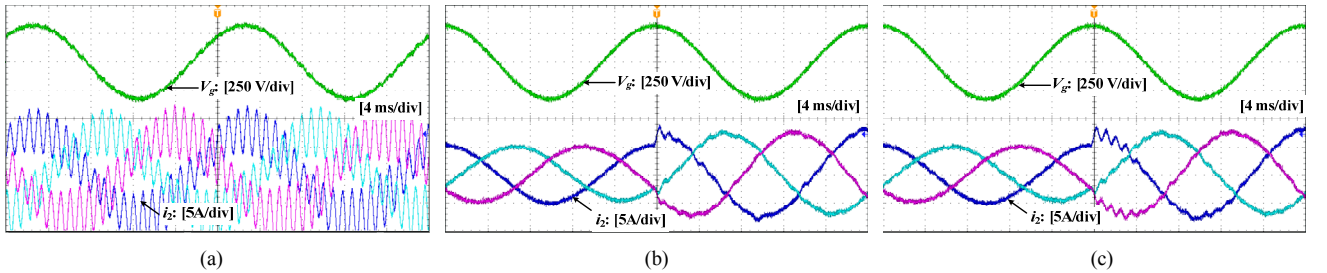
Fig. 13. Measured A-phase grid voltage and grid current for C_f = 14.1 μF, ω_{res} = 0.14ω_s. (a) k_{ad} = 5, ω_{ad} = 0.15ω_s. (b) k_{ad} = 15, ω_{ad} = 0.15ω_s. (c) k_{ad} = 15, ω_{ad} = 0.25ω_s.

in Figs. 8 to 10. The control system is implemented with a *dSPACE* DS1006 system, where a DS5101 digital waveform output speed A/D board is used to sample the PCC voltage and grid current in synchronous with the PWM pulses.

Fig. 11 shows the measured A-phase voltage and current waveforms in the case of C_f = 4.7 μF, ω_{res} = 0.24ω_s. Since the resonance frequency is above the one sixth of the sampling frequency, the system keeps stable without any damping, as shown in Fig. 11 (a), where the HPF gain k_{ad} is set to zero. However, as illustrated in Figs. 8 (b) and (c), the transient performance of the system can be enhanced with the HPF-

based active damping. To validate this conclusion, Figs. 11 (b) and (c) show the measured results with ω_{ad} = 0.35ω_s, and k_{ad} = 5 in Fig. 11 (b) and k_{ad} = 15 in Fig. 11 (c), where a step response of the current reference from 5 A to 7.5 A is tested. Compared to Fig. 11 (a), it is clear that a damping during the transient response is obtained with the HPF, and a higher k_{ad} provides a better damping performance.

Fig. 12 shows the measured phase-A voltage and current waveforms for C_f = 9.4 μF, ω_{res} = 0.17ω_s. In this case, the *LCL* resonance frequency is closes to the one-sixth of the sampling frequency. The system turns into unstable region

without damping. Fig. 12 (a) shows the resonant currents with the reduced HPF gain k_{ad}, where the system will be tripped by over-current protection if k_{ad} is further decreased. Figs. 12 (b) and (c) give a comparison for the different cutoff frequencies ω_{ad}. It can be seen that the system tends to be less damped during the transient of the step response from 5 A to 7.5 A, as shown in Fig. 12 (c). These results confirm the root loci analyses in Figs. 9 (b) and (c), where the root locus corresponding to the case of $k_{ad} = 15$, as highlighted in the red dot line, is moving outwards the unit circle by increasing the HPF cutoff frequency ω_{ad}.

Fig. 13 shows the measured waveforms for the case with the lower resonance frequency ($C_f = 14.1$ μF, $\omega_{res} = 0.14\omega_s$) than the one-sixth of the sampling frequency. Similarly to the measured results in Fig. 12, the system resonates with the reduced HPF gain k_{ad}, as shown in Fig. 13 (a). Also, for the given $k_{ad} = 15$, the less damping is produced by increasing the HPF cutoff frequency from $0.15\omega_s$ to $0.25\omega_s$, which can be observed in Figs. 13 (b) and (c). These results match with the root loci analyses in Figs. 10 (a) and (b). It is also shown that the reduced *LCL* resonance frequency requires a lower ω_{ad} to obtain a good damping with the same k_{ad}.

V. CONCLUSIONS

This paper has presented a systematic analysis and design of the grid current feedback active damping control scheme for *LCL*-filtered voltage source converters. Impedance-based analysis has revealed that this active damping loop basically synthesizes a virtual impedance in parallel with the grid-side filter inductor, which is shaped by the negative HPF with a series RL damper in parallel with a negative inductor. It is further found that the negative virtual inductor is important to avoid the non-minimum phase system induced by the transport delay in digital control system. A co-design of the current controller and active damping controller parameters has also been discussed based on the root loci analysis in the discrete *z*-domain. Experimental results obtained have shown the good steady-state and transient performance of the active damping controller based on the design guideline presented.

REFERENCES

[1] M. Liserre, F. Blaabjerg, and S. Hansen, "Design and control of an *LCL*-filter-based three-phase active rectifiers," *IEEE Trans. Ind. Appl.*, vol. 41, no. 5, pp. 1281-1291, Sept./Oct. 2005.

[2] R. N. Beres, X. Wang, F. Blaabjerg, C. L. Bak, and M. Liserre, "A review of passive filters for grid-connected voltage source converters," in *Proc. IEEE APEC* 2014, pp. 2208-2215.

[3] J. Dannehl, M. Liserre and F. Fuchs, "Filter-based active damping of voltage source converters with *LCL* filter," *IEEE Trans. Ind. Electron.*, vol. 58, no. 8, pp. 3623-3633, Aug. 2011.

[4] J. Dannehl, F. W. Fuchs, S. Hansen, and P. Thogersen, "Investigation of active damping approaches for PI-based current control of grid-connected pulse width modulation converters with LCL filters," *IEEE Trans. Ind. Appl.*, vol. 46, no. 4, pp. 1509-1517, Jul./Aug. 2010.

[5] V. Blasko and V. Kaura, "A novel control to actively damp resonance in input LC filter of a three-phase voltage source converter," *IEEE Trans. Ind. Appl.*, vol.33, no. 2, pp. 542-550, Mar./Apr. 1997.

[6] V. Miskovic, V. Blasko, T. Jahns, A. Smith, and C. Romenesko, "Observer based active damping of LCL resonance in grid connected voltage source converters," in *Proc. IEEE ECCE* 2013, pp. 4850-4856.

[7] D. Pan, X. Ruan, C. Bao, W. Li, and X. Wang, "Capacitor-current-feedback active damping with reduced computation delay for improving robustness of *LCL*-type grid-connected inverter," *IEEE Trans. Power Electron.*, vol. 29, no. 7, pp. 3414-3427, Jul. 2014.

[8] X. Wang, F. Blaabjerg, and P. C. Loh, "Design-oriented analysis of resonance damping and harmonic compensation for LCL-filtered votlage source converters," in *Proc. IEEE IPEC* 2014, pp. 216-223.

[9] S. G. Parker, B. P. McGrath, and D. G. Holmes, "Regions of active damping control for LCL filters," *IEEE Trans. Ind. Appl.*, vol. 50, no. 1, pp. 424-432, Jan./Feb. 2014.

[10] J. Dannehl, C. Wessels, and F. W. Fuchs, "Limitations of voltage-oriented PI current control of grid-connected PWM rectifiers with *LCL* filters," *IEEE Trans. Ind. Electron.*, vol. 56, no. 2, pp. 380-388, Feb. 2009.

[11] R. Teodorescu, F. Blaabjerg, M. Liserre, and A. Dell'Aquila, "A stable three-phase LCL-filter based active rectifier without damping," in *Proc. IAS* 2003, pp. 1552-1557.

[12] J. Yin, S. Duan, and B. Liu, "Stability analysis of grid-connected inverter with LCL filter adopting a digital single-loop controller with inherent damping characteristic," *IEEE Trans. Ind. Infor.*, vol. 9, no. 2, pp. 1104-1112, May 2013.

[13] X. Wang, F. Blaabjerg, and W. Wu, "Modeling and analysis of harmonic stability in an AC power-electronics-based power system," *IEEE Trans. Power Electron.*, vol. PP, no. 99, pp. 1-12, Feb. 2014.

[14] C. Dick, S. Richter, M. Rosekeit, J. Rolink, and R. De Doncker, "Active damping of LCL resonance with minimum sensor effort by means of a digital infinite impulse response filter," *Proc. EPE* 2007, pp. 1-8.

[15] M. Hanif, V. Khadkikar, W. Xiao, and J. L. Kirtley, "Two degrees of freedom active damping technique for LCL filter based grid connected PV systems," *IEEE Trans. Ind. Electron.*, vol. 61, no. 6, pp. 2795-2803, Jun. 2014.

[16] J. Xu, S. Xie and T. Tang, "Active damping-based control for grid-connected LCL-filtered inverter with injected grid current feedback only," *IEEE Trans. Ind. Electron.*, vol. 61, no. 9, pp. 4746-4758, Sept. 2014.

[17] S. Chung, "A phase tracking system for three phase utility interface inverters," *IEEE Trans. Power Electron.*, vol. 15, no. 3, pp. 431-438, May 2000.

[18] T. Messo, J. Jokipii, A. Makinen, T. Suntio, "Modeling the grid synchronization induced negative-resistor-like behavior in the output impedance of a three-phase photovoltaic inverter," in *Proc. IEEE PEDG* 2013, pp.1-8.

[19] S. Buso and P. Mattavelli, *Digital Control in Power Electronics*, San Francisco, CA: Morgan & Claypool Publ., 2006.

[20] A. G. Yepes, F. Freijedo, O. Lopez, and J. Gandoy, "High-performance digital resonant controllers implemented with two integrators," *IEEE Trans. Power Electron.*, vol. 26, no. 2, pp. 563-576, Feb. 2011.

[21] D. G. Holmes, T. A. Lipo, B. P. McGrath, and W. Y. Kong, "Optimized design of stationary frame three phase AC current regulators," *IEEE Trans. Power Electron.*, vol. 24, no. 11, pp. 2417-2426, Nov. 2009.